ORIGINAL PAPER

A wide axial-ratio beamwidth circularly-polarized oval patch antenna with sunlight-shaped slots for gnss and wimax applications

Ahmad Abdalrazik[1] · Ahmed Gomaa[2] · Ahmed A. Kishk[3]

Abstract
This paper proposes a quadruple band stacked oval patch antenna with sunlight-shaped slots supporting L1/L2/L5 GNSS bands and the 2.3 Ghz WiMAX band. The antenna produces right-hand circular polarization waves with wide axial-ratio beamwidth of 223/216° and 231/203° at two orthogonal cutplanes at L5 and L2 GNSS bands, respectively. Firstly, the resonant modes TM_{110} and TM_{210} are excited inside a single layer oval patch antenna, where resonance frequencies are calculated using Mathieu functions. Meanwhile, it is shown that another version of the mode TM_{110} with similar distribution but orthogonal direction is excitable inside the same oval patch. Then, a second stacked oval patch layer is added, which splits the resonance frequency of each of the modes TM_{110} and TM_{210} into two different values. Depending on the probe feed position and the separation between the two layers, the phase shifts between modes versions in the upper and the lower layers change. Thus, by fine-tuning the probe feed position and the separation between layers, spatially-orthogonal with quadrature-phase-shift versions of the mode TM_{110} are obtained, producing a circularly polarized waves at L2 and L5 bands. Furthermore, sunlight shaped slots are etched into the upper and lower layer patches to fine tune the phase shifts between different modes versions, which enhances the overall axial-ratio beamwidth. Despite the simplicity of the overall structure and the feeding mechanism utilized in the proposed design, wide axial-ratio beamwidths are obtained, as compared to previous works. The proposed antenna shows low reflection coefficient values at 1.14–1.29 GHz (L2/L5), 1.45–1.6 GHz (L1), and 2.26–2.4 GHz (WiMAX). The antenna gains are 5.9, 5.6, 6, and 6.5 dBi/dBic at L5, L2, L1, and WiMAX bands, respectively. The half-power beamwidths are 99/96°, 102/96°, 112/85°, and 65/48° at two orthogonal cutplanes at L5, L2, L1, and WiMAX bands, respectively.

Keywords Circular polarization · GNSS antenna · Mathieu function · multiband antenna

✉ Ahmad Abdalrazik
  ahmadabdalrazik@eng.psu.edu.eg

  Ahmed Gomaa
  ahmed.gomaa@nriag.sci.eg

  Ahmed A. Kishk
  kishk@encs.concordia.ca

[1] Electrical Engineering Department, Faculty of Engineering, Port Said University, Port Said 42524, Egypt

[2] National Research Institute of Astronomy and Geophysics (NRIAG), Helwan 11421, Egypt

[3] Department of Electrical and Computer Engineering, Concordia University, Montreal, QC H3G 2W1, Canada

1 Introduction

Currently, Global Navigation Satellite System (GNSS) provides the fastest and most robust means for positioning, navigation and timing (PNT) applications. Indeed, it plays a unique role in transportation, construction, agriculture, communications, sensing, and more. The GNSS includes different constellations of earth-orbiting satellites that broadcast their locations in space and time, working together with a network of ground control stations/receivers that calculate ground positions through a specific version of trilateration. Like all other communication systems, continuous efforts are being exerted to upgrade and modernize GNSS systems to cope with modern world communication systems requirements such as high

precision, performance-stability, robustness, affordability, and energy-effectiveness.

In any GNSS receiver device, the antenna is the element that is responsible for receiving the wireless satellite signals. As such, the GNSS antennas should meet certain requirements to receive the satellite signal effectively and enable the GNSS receiver device to function reliably. Generally, GNSS antennas should provide high gain beampatterns with low backlobe radiation patterns to minimize the reception of interference and multipath signals that result in positioning errors. Furthermore, it should have low reflection coefficient values at the largest possible number of the available GNSS bands.

Also, the GNSS wireless signals are received in the right hand (RH) circularly polarized (CP) mode, which effectively combats multi-path interference, polarization mismatch, and distortions due to transmitter-receiver respective orientations mismatch [1]. Thus, one of the most important features that describe the performance of signal coverage in any GNSS receiver antenna is the ability of operation in RHCP mode with wide axial ratio beamwidth (ARBW), to be able to receive the CP signals at low elevations close to the horizon. Furthermore, wide ARBW is an essential requirement for the geostationary satellite receiver antennas used at high latitudes to secure enough communication links [2].

In this context, many recent GNSS antenna designs with wide axis-ratio beamwidth (ARBW) were presented [3–9]. For instance, Zhang et al. [3] presented a wide-beam circularly polarized cross-dipole antenna for GNSS applications. The dipole arms' lengths are fine tuned to obtain the circularly polarized radiation. Also, slots are etched into the ground to enhance the reflection coefficient bandwidth. To further enhance the ARBW characteristics, the dipole arms were curved, and the distance between them and the metallic ground plane was fine tuned. The antenna provides ARBW as wide as 148 ° at the L1 GNSS band. Another wide ARBW antenna design was reported in [4], where the authors proposed a dual-band antenna consisting of two stacked patches and backed by a metallic cavity. The structure of the metallic cavity is modified to widen the 3-dB ARBW at two operating bands. Also, four pillars are inserted closely to the lower patch layer to minimize the overall structure size. The antenna provides ARBWs of 108° and 107° at L1 and L2 bands, respectively. Also, a more recent design [5] presented a dual-band printed quadrifilar helix antenna with wide beamwidth for GPS applications. The antenna provides ARBWs of 126° and 120° at L1 and L2 bands, respectively.

Recently, the research studies on the GNSS receivers that operate over the new L5 GNSS band have revealed promising outcomes [10–12]. For instance, it has been shown that GNSS signal transmission over the L5 band results in a superior received signal strength performance and improved accuracy, as compared to the L1 band transmission. Also, the L5 band is broadcasted at a higher power level than the L2C and legacy L1 C/A signals, which provides better received signal precision. In addition, since a wider bandwidth is allocated to the L5 band as compared to L1 band, it shows a better interference mitigation performance. Furthermore, it has been shown that the combined usage of any two bands of L1, L2 and L5 bands provides an enhanced level of performance robustness. Moreover, GNSS signals transmitted over L5 band possess a higher received effective power than L1 and L2 bands, which provides an enhanced fringe visibility and less susceptibility to environment noise. Despite the discussed advantages of utilizing the L5 band in modern GNSS systems, only few works have addressed the development of GNSS antennas operating in L5 band [13, 14]. However, the aforementioned works show narrow ARBW/half-power-beamwidth (HPBW) performance.

In this paper, a stacked patch antenna with sunlight-shaped slots is proposed. The proposed design produces an ARBW as wide as 223/216° and 231/203° at two orthogonal cutplanes at L5 and L2 bands, respectively, which is wider than many previous works [3–9]. Also, despite the wide ARBW, the proposed antenna structure is fed directly by a single probe, without the need for neither bulky backing cavities, external feeding networks, nor three-dimensional complicated fabrication design of curved dipole arms, as compared to [3–6, 8]. Moreover, the proposed printed antenna is fabricated through the printed circuit board technology, offering simplicity of fabrication and cost reduction, contrarily to helix/wire antennas [5]. The proposed antenna shows a low reflection coefficient at 1.14–1.29 (L2/L5), 1.45–1.6 (L1), and 2.26–2.4 GHz (WiMAX). In fact, increasing the number of operating GNSS bands not only enables effective correction for ionosphere errors in real-time kinematic (RTK) applications, but also reduces the complexity of the radio-frequency (RF) front-end [4, 15]. The HPBWs of radiated patterns are 107/87°, 89/109°, 107/81°, and 110/61°, with gains of 5.9 dBic, 5.6 dBic, 6 dBi, and 6.5 dBi at two orthogonal cutplanes at L5, L2, L1, and WiMAX bands, respectively.

2 Proposed antenna

2.1 Antenna structure

As shown in Fig. 1, the proposed antenna consists of two stacked FR4 substrates with a dielectric constant of 4.3 and an area of 79*122.8 mm^2, where the upper and lower substrates' thicknesses are 11.2 and 3.2 mm, respectively.
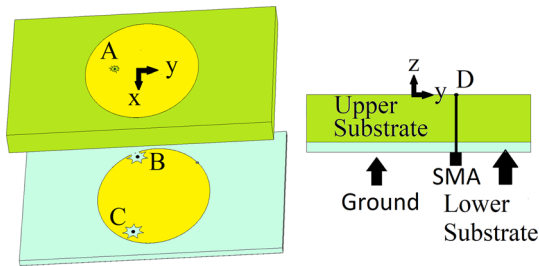
Fig. 1 Proposed antenna structure. All dimensions are in mm. A = $(-2, -12.6,)$, B = $(-26.4, -8.5, -11.2)$, C = $(24.1, -8.5, -11.2)$, and D = $(-21.1, 19.8, 0)$

Each substrate is topped by an oval patch with major and minor axes of 32 and 26.5 mm, respectively. A probe feeds the stacked structure at the point D as depicted in Fig. 1. Moreover, one sunlight-shaped slot centered at point A is etched in the upper patch metal; and two sunlight-shaped slots centered at points B and C, are etched in the lower patch metal. Each of the proposed antenna's sunlight-shaped slots can be described using the following two-dimensional Gielis's generalized super-ellipse formula [16],

$$r(\varphi) = \left(\left| \frac{\cos\left(\frac{m\varphi}{4}\right)}{a} \right|^{n_2} + \left| \frac{\sin\left(\frac{m\varphi}{4}\right)}{b} \right|^{-\frac{1}{n_1}} \right) \tag{1}$$

where φ is the circular coordinate angle measured from the x-axis, and m, n_1, n_2, n_3, a, and b are all positive constants. The upper slot is defined by the parameters m = 21.2, n_2=2.6, n_3 = 18.7, n_1= 14.96, a = 8.9, b = 5.3, and each of the lower slots is defined by the parameters m = 14.1, n_2= 5.3, n_3 = 10.3, n_1 = 17.3, a = 31.2, b = 15.6.

2.2 Modes analysis

According to the cavity model of elliptical patch antenna, bottom and top walls are considered as perfect electric conductors, while side walls are considered as perfect magnetic conductors. For a TM mode, the longitudinal component, E_z, wave equation can be written in elliptical coordinates, ξ and η, as follows [17]

$$\frac{1}{\rho^2 \left(\cosh^2 \xi - \cos^2 \eta \right)} \left(\frac{\partial^2 E_z}{\partial \xi^2} + \frac{\partial^2 E_z}{\partial \eta^2} \right) + k^2 E_z = 0 \tag{2}$$

where ρ is the focal distance of the ellipse. By assuming a solution of the form $E_z = R(\xi)\Phi(\eta)$, it is found that $\Phi(\eta)$ and $R(\xi)$ must satisfy

$$\frac{d^2\Phi}{d\eta^2} + (a - 2\,q\,\cos 2\eta)\Phi = 0 \tag{3}$$

$$\frac{d^2 R}{d\xi^2} - (a - 2\,q\,\cosh 2\xi)R = 0 \tag{4}$$

where $q = \rho^2 k_T^2 / 4$, $k_T = k^2 - k_z^2$, and a is a separation constant arising from the separation of variables method. The above equations are known as the angular and radial Mathieu equations, respectively. By applying the boundary condition of side magnetic walls at $\xi = \xi_0$, the transcendental equation $R(q, \xi_0) = 0$ is solved to find the resonance frequency of the TM_{mnp} mode, as follows,

$$f_{mnp} = \frac{v}{2\pi} \sqrt{\frac{4q_{mn}}{\rho^2} + \left(\frac{p\pi}{d}\right)^2} \tag{5}$$

where q_{mn} is the nth root of the m-degree Radial Mathieu function $R_m(q, \xi_0)$, v is the wave velocity inside the substrate of thickness d.

Based on the previous model, an oval patch with major and minor axes of 32 and 26.5 mm generates the two modes TM_{110} and TM_{210} at 1.3 and 2.1 GHz. We simulate this single layer oval patch, and the results are shown in Fig. 2. It can be seen that the modes TM_{110} and TM_{210} resonate at 1.4 and 2.3 GHz, respectively, which means the theoretically calculated modes' resonances frequencies are close to simulation results. Also, the modes TM_{110} and TM_{210} surface currents are given in Fig. 2(a).

In fact, the mode TM_{110} can be excited while being accompanied by a corresponding orthogonal version of the same distribution [18, 19], where the phases of the accompanying surface currents version depend on the
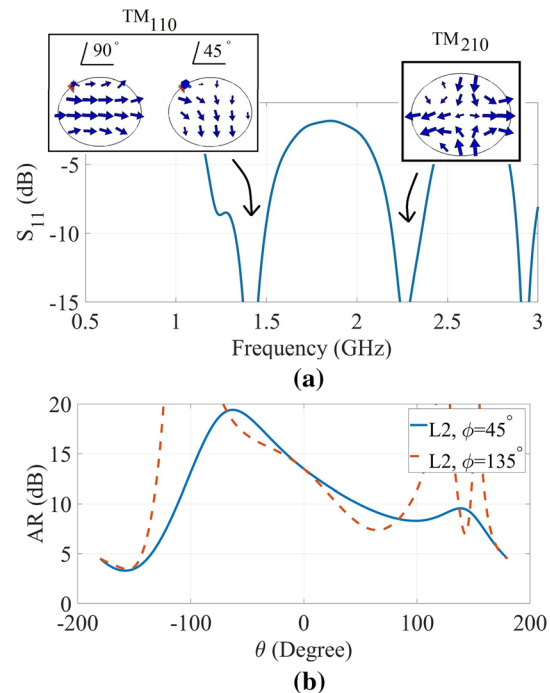
Fig. 2 **a** S_{11} and **b** AR response for single layer patch antenna

probe feed position [20]. It is found that due to a feed probe position at point D, a 45° phase shift between the two orthogonal versions of mode TM_{110} surface currents is obtained, as shown in Fig. 2a. As will be discussed shortly, these two orthogonal versions will be modified and utilized to produce CP waves. Also, it is worth mentioning that the feed point is initially chosen at the diagonal of the oval patch to ease the excitation of the modes TM_{110} and TM_{210} at different phases.

According to the oval patch cavity model, the field distribution for a mode TM_{nmp} with $p = 0$ does not vary along the z direction, meaning that the field distribution for a mode with $p = 0$ always possesses the same pattern at any arbitrary plane $z = z_0$. Thus, if a new identical oval patch element is stacked beneath the prescribed single-layer oval patch antenna, the same surface currents of the modes, TM_{110} and TM_{210}, will be still generated at each oval patch element. To show this, we simulate a stacked dual layer oval antenna structure, such that the upper and lower oval patches lie at heights z = 14.4 and 3.2mm, respectively. The

simulated s_{11} for this stacked double structure is shown in Fig. 3(a). By comparing s_{11} response for single and dual oval patch structures, i.e. Figs. 2(a) and 3(a), it is noticed that mode frequency splitting occurs in the dual oval patch structures, meaning that each mode's resonance frequency

splits into two new frequencies. Frequency splitting is a known phenomenon that occurs when power couples between two resonant structures, i.e. the two stacked patches [21, 22]. Moreover, it is noticed from Fig. 3a that the mode TM_{110} surface currents are still excited at both spitted frequencies 1.2 (L2) and 1.5 GHz (L1) at both upper and lower layers. Since the feed location did not change, the structure preserves the phase shift between the two orthogonal modes at 45° at each layer. Also, the mode TM_{210} surface currents are excited at 2.3 GHz (WiMAX). It is worth mentioning that the probe feeds the upper patch layer directly, while the lower patch is proximity-coupled by the upper layer for a reason that will be clearer in the next subsection.

2.3 Circular polarization analysis

As discussed earlier, the upper and lower patches are identical, generating the orthogonal versions of mode TM_{110} surface currents identically in each patch. Also, since the probe feeds the upper patch directly which, in turn, couples power to the lower patch by proximity, the mode TM_{110} surface currents generated in the lower layer are slightly phase-delayed behind surface currents in the upper patch. Thus, by changing the separation between the upper and lower layers, the phase delay between the upper and lower surface currents varies. It is found that a separation of 11.2 mm between the two layers results in ∼ 45° phase shift between the upper and lower surface currents at 1.3 GHz. This is because a separation of

11.2 mm is approximately equivalent to $\lambda_g/8$ at 1.3 GHz. Consequently, the phases of the mode TM_{110} versions at the upper and lower layers are 45°, 90°, 135°, and 180° as depicted in Fig. 3a.

Thus, it is noted that the surface current distribution of each version of the mode TM_{110} excited in the upper layer possesses a corresponding orthogonal version with a 90° phase shift excited in the lower layer. Hence, the two-layers structure is expected to produce CP waves, which can be verified by comparing the AR responses at L2 band in cases of single- and dual-layers structures, as in Fig 2b and 3(b), where low values of AR are observed at the broadside in Fig. 3(b). It is also noticed that the dimensions of the dual layer oval structure are suitable to preserve the orthogonality between the TM_{110} mode surface currents versions at L5 band, resulting in low values of AR as shown in Fig 3(b). The ARBWs of the dual layer structure are 223/153° and 215/173° at two diagonal cutplanes at L5 and L2 bands, respectively.

Interestingly, it is found that further ARBW improvements can be achieved by placing two sets of sunlight-shaped slots in the upper and lower layers. The optimized
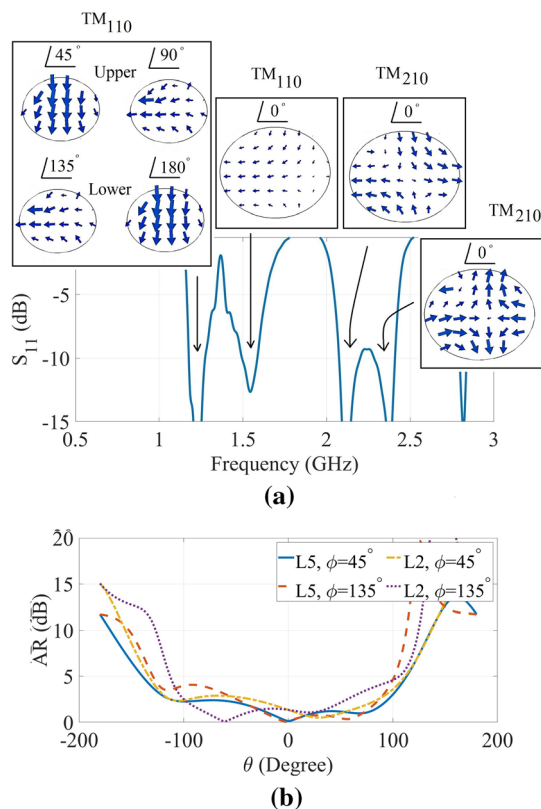
Fig. 3 a S_{11} and b AR response for double layer patch antenna

slots' shapes, dimensions and positions are given in Fig. 1 and Subsection 2.1. These additional slots fine tune phase delay values between different versions of the mode TM_{110} surface currents, such that better CP and ARBW performance are obtained, where AR performance is given in Fig 4. The ARBWs of the slotted dual layer structure are 223/216° and 231/203° at two diagonal cutplanes at L5 and L2 bands, respectively. Parametric study of the dimensions and positions of the proposed sunlight-shaped slots are given in the next subsection.

2.4 Parametric study

As discussed earlier, the slots positions and sizes are optimized to enhance ARBW by fine tuning the orthogonality and the phase shifts between surface currents versions of the mode TM_{110} to obtain CP operation at L2 and L5 bands. To show the importance of the optimized sizes of slots, we present in Fig. 5a and b, respectively, the AR performance for the proposed structure with lower slots double- and half-sized, where degraded AR performance is noticed. However, less degradation in AR performance is seen in the case of reducing slots sizes. This is attributed to the fact that small slot sizes have only a small effect on the lengths and phases of TM_{110} surface currents. In fact, with total removal of slots, the proposed dual-layer oval patch is able to show a good AR performance, as given in Fig. 3b. To obtain a better AR performance than the one given in Fig. 3b, the optimized values of slots sizes given in Sect. 2.1 are required, so as to obtain the AR performance given in Fig. 4.

Also, the separation between the two layers plays an important role in producing quadrature phase shift between the upper and lower orthogonal versions of TM_{110} surface currents. To show this, we present in Fig. 6 the AR performance for different separation values, where it can be seen that applying variations to the optimized 11.2mm-separation does change the required 90 ° phase shift for CP operation, degrading the AR performance at L2 and L5 bands, as compared to the optimized AR performance given in Fig. 4.
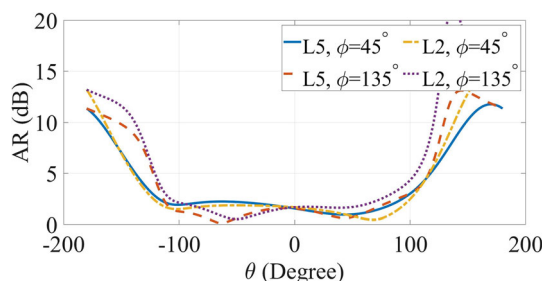

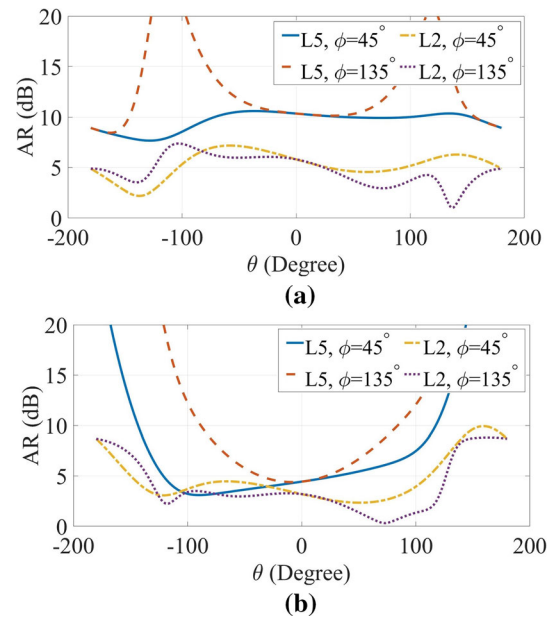**Fig. 4** AR reponse for the proposed antenna

Fig. 5 Simulated axial ratio at L5 and L2 bands with lower slots scaled to **a** double sizes **b** half sizes
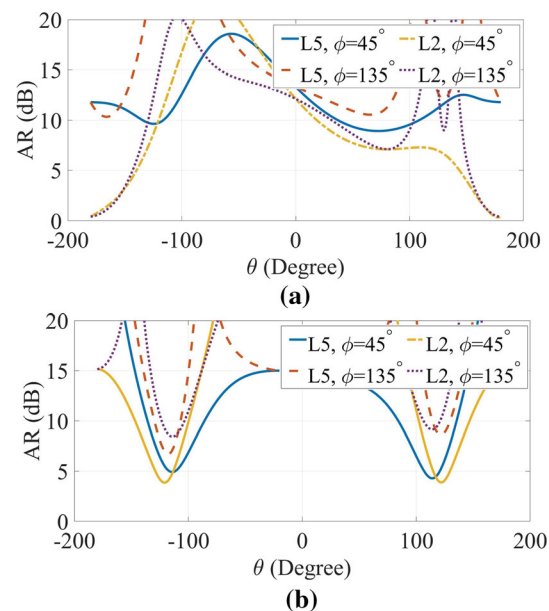

Fig. 6 Simulated axial ratio at L5 and L2 bands with dual-layers-separation of **a** 19.2 mm, **b** 3.2 mm

3 Fabrication and measurements

The antenna was fabricated as shown in Fig. 7 and measured using R&S®ZVB Vector Network Analyzer and anechoic chamber. The measured reflection coefficient response is shown in Fig. 8, where good agreement between simulated and measured results is noted. The measured -10 dB reflection coefficient bandwidths are
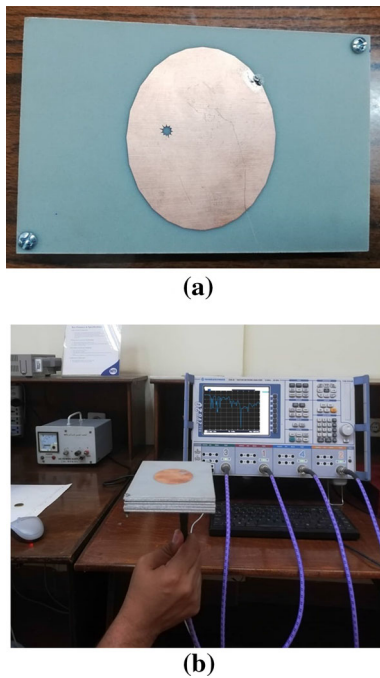
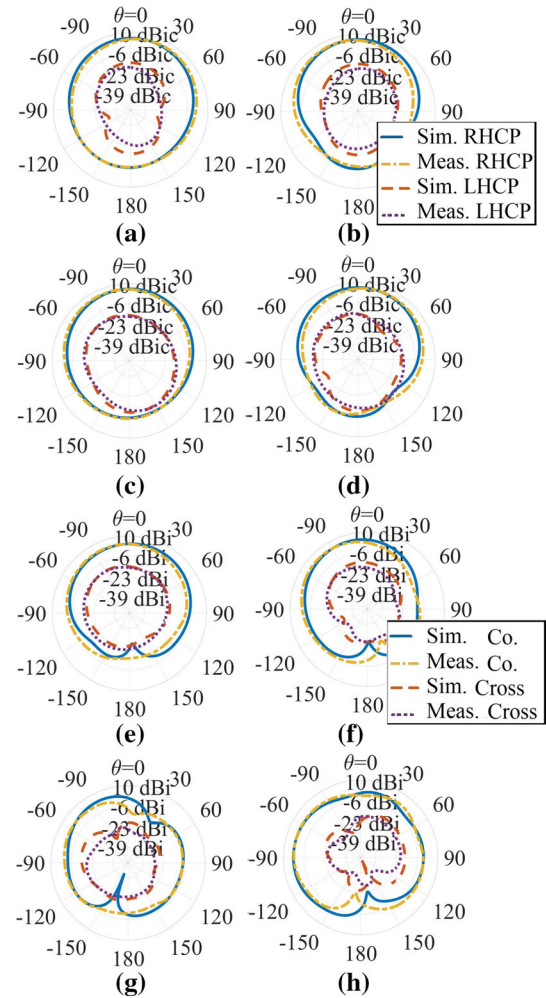**Fig. 7 a** Prototype of the fabricated antenna. **b** measurement of S_{11}
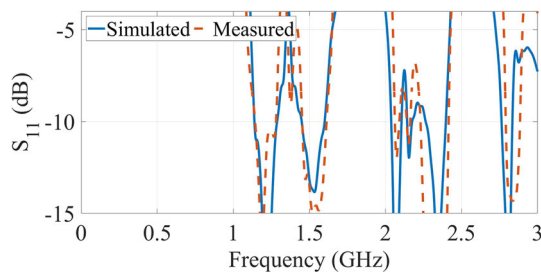
Fig. 8 Simulated and measured S_{11} response for the proposed antenna

Fig. 9 Simulated and measured RHCP/LCHP/co./cross patterns at **a** L5, $\phi = 45°$, **b** L5, $\phi = 135°$, **c** L2, $\phi = 45°$, **d** L2, $\phi = 135°$, **e** L1, $\phi = 45°$, **f** L1, $\phi = 135°$, **g** WiMAX, $\phi = 45°$, **h** WiMAX, $\phi = 135°$

1.14-1.29 GHz (L2/L5), 1.45-1.6 GHz (L1), and 2.26-2.4 GHz (WiMAX).

The antenna radiates RHCP waves as required by the GNSS system. The RH and LH patterns are shown in Fig. 9. Antenna gains are 5.9, 5.6, 6, and 6.5 dBi/dBic at L5, L2, L1, and WiMAX bands, respectively. The measured half power beamwidths are 100/93°, 104/96°, 103/85°, and 79/48° at two orthogonal cutplanes at L5, L2, L1, and WiMAX bands, respectively.

Also, we show in Table 1 a performance comparison between the proposed antenna and previous works. By inspecting the previous works shown in the table, it is noticed that some designs show relatively wide ARBWs. However, this usually comes on the expense of narrower HPBW, e.g. compare [5] vs [6], or at the expense of smaller number of operating bands, e.g. compare [6] vs [8]. In the same context, our proposed design shows the highest values of ARBWs for a dual-RHCP-bands GNSS operation, with relatively good values of HPBWs, and fair size.

Moreover, the proposed antenna possesses low reflection coefficient values at L1 GNSS band. In fact, increasing the number of operating GNSS bands in our proposed design to three, has a positive impact not only enables effective correction for ionosphere errors in real-time kinematic (RTK) applications, but also reduces the complexity of the radio-frequency (RF) front-end [4, 15]. Also, despite the wide ARBW, the proposed antenna structure is fed directly by a single probe, without the need for neither bulky backing cavities, external feeding networks, nor three-dimensional complicated fabrication design of dangled dipole arms, as compared to [3–6, 8]. Moreover, the proposed antenna is fabricated through the printed circuit board technology, which offers cost reduction and ease of fabrication, contrarily to wire/helix antennas [5].

Table 1 Performance comparison to previous works

References	s_{11} bands	Smallest ARBW (°)	SmallestHPBW (°)	No. ofbands	Simple design/ w/o ext. feed net.	Size (mm)
[5]	L1/ L2	186, 163	126, 120	2	No	60*60*18.5
[4]	L1/ L2	170, 130	108, 107	2	No	70*70*20
[3]	L1	150	148	1	No	160*160*80
[6]	L1/ L2	200,210	103,111	2	No	150*150*72
[7]	L1	60	60	1	Yes	50*37*5.8
[8]	L1	230	150	1	No	150*150*70
[9]	L1	188	30	1	Yes	90*90*3
Prop- osed work	L1/L2/ L5/ WiMAX	216, 203	96,96, 85,48	4	Yes	79*122*14.4

4 Conclusion

A stacked oval patch operating at L1/2/5 GNSS and 2.3 GHz WiMAX bands, was proposed in this paper. The stacked oval structure produces RHCP waves with wide axial ratio beamwidth of 223/216° and 231/203° at two diagonal cutplanes at L5 and L2 GNSS bands, respectively. Mathieu functions were utlized to obtain resonance frequencies of modes TM_{110} and TM_{210} excited inside an oval patch antennas. The structure dimensions were fine tuned such that orthogonal versions of the mode TM_{110} is obtained. Furthermore sunlight shaped slots were added and optimized to enhance the arbw. The antenna was fabricated and measured and the antenna shows low reflection coefficient values at 1.14–1.29 GHz (L2/L5), 1.45–1.6 GHz (L1), and 2.26–2.4 GHz (WiMAX). The antenna gains are 5.9, 5.6, 6, and 6.5 dBi/dBic at L5, L2, L1, and WiMAX bands, respectively. The half power beamwidths are 99/96°, 102/96°, 112/85°, 65/48° at two orthogonal cutplanes at L5, L2, L1, and WiMAX bands, respectively.

Data availibility The datasets supporting the conclusions of this article are included within the article.

References

1. Mak, K. M., & Luk, K. M. (2009). A circularly polarized antenna with wide axial ratio beamwidth. *IEEE Transactions on Antennas and Propagation, 57*(10), 3309–3312.
2. Liu, S., Yang, D., & Pan, J. (2019). A low-profile circularly polarized metasurface antenna with wide axial-ratio beamwidth. *IEEE Antennas and Wireless Propagation Letters, 18*(7), 1438–1442.
3. Zhang, Y. Q., Qin, S. T., Li, X., & Guo, L. X. (2018). Novel wide-beam cross-dipole cp antenna for gnss applications. *International Journal of RF and Microwave Computer-Aided Engineering, 28*(6), e21272.
4. Zhong, Z. P., Zhang, X., Liang, J. J., Han, C. Z., Fan, M. L., Huang, G. L., Xu, W., & Yuan, T. (2019). A compact dual-band circularly polarized antenna with wide axial-ratio beamwidth for vehicle gps satellite navigation application. *IEEE Transactions on Vehicular Technology, 68*(9), 8683–8692.
5. Liu, H., Shi, M., Fang, S., & Wang, Z. (2020). Design of low-profile dual-band printed quadrifiliar helix antenna with wide beamwidth for uav gps applications. *IEEE Access, 8*, 157,541-157,548.
6. Sun, Y. X., Leung, K. W., & Ren, J. (2018). Dual-band circularly polarized antenna with wide axial ratio beamwidths for upper hemispherical coverage. *IEEE Access, 6*, 58132–58138.
7. Sundarsingh, E. F., Harshavardhini, A., et al. (2019). A compact conformal windshield antenna for location tracking on vehicular platforms. *IEEE Transactions on Vehicular Technology, 68*(4), 4047–4050.
8. Sun, Y. X., Leung, K. W., & Lu, K. (2017). Broadbeam cross-dipole antenna for gps applications. *IEEE Transactions on Antennas and Propagation, 65*(10), 5605–5610.
9. Wang, M. S., Zhu, X. Q., Guo, Y. X., & Wu, W. (2018). Compact circularly polarized patch antenna with wide axial-ratio beamwidth. *IEEE Antennas and Wireless Propagation Letters, 17*(4), 714–718.
10. Saleem, T., Usman, M., Elahi, A., & Gul. N. (2017). Simulation and performance evaluations of the new GPS L5 and L1 signals. *Wireless Communications and Mobile Computing, 2017*, 1–4. https://doi.org/10.1155/2017/7492703
11. Tabibi, S., Nievinski, F. G., van Dam, T., & Monico, J. F. (2015). Assessment of modernized gps l5 snr for ground-based multipath

reflectometry applications. *Advances in Space Research, 55*(4), 1104–1116.

12. Paziewski, J., Fortunato, M., Mazzoni, A., & Odolinski, R. (2021). An analysis of multi-gnss observations tracked by recent android smartphones and smartphone-only relative positioning results. *Measurement, 175*(109), 162.

13. Che, J. K., Chen, C. C., & Locke, J. F. (2021). A compact cavity-backed tri-band antenna design for flush mount gnss (l1/l5) and sdars operations. *IEEE Antennas and Wireless Propagation Letters, 20*(5), 638–642.

14. Hussine, U.U., Huang, Y., & Song, C. (2017). in 2017 11th European Conference on Antennas and Propagation (EUCAP) (IEEE, 2017), pp. 1954–1956.

15. Rao, B. R., McDonald, K., & Kunysz, W. (2013). *GPS/GNSS Antennas*. US: Artech House.

16. Matsuura, M. (2015). Gielis' superformula and regular polygons. *Journal of Geometry, 106*(2), 383–403.

17. Gutiérrez-Vega, J. C., Rodrıguez-Dagnino, R., Meneses-Nava, M., & Chávez-Cerda, S. (2003). Mathieu functions, a visual approach. *American Journal of Physics, 71*(3), 233–242.

18. Kumar, C., & Guha, D. (2011). Nature of cross-polarized radiations from probe-fed circular microstrip antennas and their suppression using different geometries of defected ground structure (dgs). *IEEE Transactions on Antennas and Propagation, 60*(1), 92–101.

19. Samanta, S., Reddy, P. S., & Mandal, K. (2018). Cross-polarization suppression in probe-fed circular patch antenna using two circular clusters of shorting pins. *IEEE Transactions on Antennas and Propagation, 66*(6), 3177–3182.

20. Li, Q., Li, W., Zhu, J., Zhang, L., & Liu, Y. (2020). Implementing orbital angular momentum modes using single-fed rectangular patch antenna. *International Journal of RF and Microwave Computer-Aided Engineering, 30*(5), e22165.

21. Mateo-Segura, C., Feresidis, A. P., & Goussetis, G. (2013). Bandwidth enhancement of 2-d leaky-wave antennas with double-layer periodic surfaces. *IEEE Transactions on Antennas and Propagation, 62*(2), 586–593.

22. Pance, K., Viola, L., & Sridhar, S. (2000). Tunneling proximity resonances: interplay between symmetry and dissipation. *Physics Letters A, 268*(4–6), 399–405.